

High-Performance Aqueous Zinc–Ion Battery Based on Layered $\text{H}_2\text{V}_3\text{O}_8$ Nanowire Cathode

Pan He, Yueli Quan, Xu Xu, Mengyu Yan,* Wei Yang, Qinyou An, Liang He, and Liqiang Mai*

Rechargeable aqueous zinc–ion batteries have offered an alternative for large-scale energy storage owing to their low cost and material abundance. However, developing suitable cathode materials with excellent performance remains great challenges, resulting from the high polarization of zinc ion. In this work, an aqueous zinc–ion battery is designed and constructed based on $\text{H}_2\text{V}_3\text{O}_8$ nanowire cathode, $\text{Zn}(\text{CF}_3\text{SO}_3)_2$ aqueous electrolyte, and zinc anode, which exhibits the capacity of $423.8 \text{ mA h g}^{-1}$ at 0.1 A g^{-1} , and excellent cycling stability with a capacity retention of 94.3% over 1000 cycles. The remarkable electrochemical performance is attributed to the layered structure of $\text{H}_2\text{V}_3\text{O}_8$ with large interlayer spacing, which enables the intercalation/de-intercalation of zinc ions with a slight change of the structure. The results demonstrate that exploration of the materials with large interlayer spacing is an effective strategy for improving electrochemical stability of electrodes for aqueous Zn ion batteries.

The deterioration of the environment and the depletion of resources call for renewable energy sources such as solar, wind power, and tide energy, but these sorts of energy require the cooperation of energy storage devices since they highly rely on time and location.^[1,2] Among various energy storage systems, lithium–ion batteries (LIBs) still play an important role in markets, but their further development is hindered by high-cost as well as some safety concerns.^[3–6] Recently, rechargeable multivalent ion batteries have been receiving much attention, such as zinc–ion batteries (ZIBs), aluminum ion batteries

(AIBs), and magnesium ion batteries (MIBs), as they deliver high volumetric energy density (based on the metal anode, Zn: $5851 \text{ mA h mL}^{-1}$, Al: $8046 \text{ mA h mL}^{-1}$, Mg: $3833 \text{ mA h mL}^{-1}$).^[7–12] Interestingly, zinc anode has a higher redox potential ($E^0 = -0.76 \text{ V}$ vs standard hydrogen electrode) compared with other metal anodes, ensuring it is applicable to aqueous battery system. As a result, the environmental pollution as well as cost can be greatly reduced by using aqueous electrolyte to take the place of traditional organic electrolyte. Combining with the advantages of safety, abundance of zinc source and environmental friendliness, it is of great significance to develop high-performance aqueous ZIBs for large-scale energy storage.^[13–16]

Cathode materials with intercalation reaction occupy a predominant position in ZIBs, many popular materials including MnO_2 , Prussian blue analogue, ZnMn_2O_4 and V_2O_5 belong to the category of intercalation.^[17–22] Besides V_2O_5 , many other layered vanadium compounds, such as $\text{Zn}_{0.25}\text{V}_2\text{O}_5 \cdot n\text{H}_2\text{O}$,^[16] VS_2 ,^[23] and LiV_3O_8 ,^[24] can also act as promising host materials for ZIBs based on intercalation reaction. Vanadium oxide hydrate, belonging to the family of layered vanadium compounds, is formulated as $\text{H}_2\text{V}_3\text{O}_8$ instead of $\text{V}_3\text{O}_7 \cdot \text{H}_2\text{O}$, since it better describes the water molecule in the crystal structure. $\text{H}_2\text{V}_3\text{O}_8$ is comprised of V_3O_8 layers linked by hydrogen bonds, and each layer consists of VO_6 octahedra and VO_5 trigonal bipyramids (Figure S1, Supporting Information). VO_6 octahedra share edges with the adjacent one piled along *c*-axis and share corners with edge-shared VO_5 trigonal bipyramids, forming a layer parallel to (100) plane. In addition, hydrogen atoms are bonded to oxygen atom labeled O(6) in VO_6 octahedra forming hydrogen bonds and holding V_3O_8 layers thus yielding a 3D structure.^[25] In this structure, V^{5+} and V^{4+} coexist with the ratio of 2:1, and the mixed valence of vanadium contributes to a higher electrical conductivity compared with other vanadium oxides.^[26] It is believed that the weak-bonded hydrogen bonds between V_3O_8 layers favor reversible insertion/extraction of ions.^[27] There are many reports about vanadium compounds acting as electrode materials,^[28,29] and there is no exception with $\text{H}_2\text{V}_3\text{O}_8$. Although there are several reports about $\text{H}_2\text{V}_3\text{O}_8$ as electrode materials for LIBs^[26,27,30] and sodium-ion batteries,^[31] to the best of our knowledge, there is no report about the zinc–ion storage of $\text{H}_2\text{V}_3\text{O}_8$ for aqueous ZIBs.

Herein, a new and high-performance ZIB system is designed based on $\text{H}_2\text{V}_3\text{O}_8$ nanowire cathode, a zinc anode

P. He, Y. L. Quan, Dr. X. Xu, Dr. M. Y. Yan, W. Yang, Prof. Q. Y. An, Prof. L. He, Prof. L. Q. Mai
State Key Laboratory of Advanced Technology
for Materials Synthesis and Processing
Wuhan University of Technology
Wuhan 430070, P. R. China
E-mail: ymymiles@whut.edu.cn; mlq518@whut.edu.cn

M. Y. Yan
Department of Materials Science and Engineering
University of Washington
Seattle, WA 98195-2120, USA

L. He
Department of Materials Science and NanoEngineering
Rice University
Houston, TX 77005, USA

L. Q. Mai
Department of Chemistry
University of California
Berkeley, CA 94720, USA

 The ORCID identification number(s) for the author(s) of this article can be found under <https://doi.org/10.1002/smll.201702551>.

DOI: 10.1002/smll.201702551

and 3 M $\text{Zn}(\text{CF}_3\text{SO}_3)_2$ electrolyte, as illustrated in **Figure 1a**. The $\text{Zn}/\text{H}_2\text{V}_3\text{O}_8$ battery delivers a high specific capacity of $423.8 \text{ mA h g}^{-1}$ at the current density of 0.1 A g^{-1} and a high capacity retention of 94.3% after 1000 cycles at 5.0 A g^{-1} . The electrochemical performances and electrochemical kinetics of $\text{H}_2\text{V}_3\text{O}_8$ electrodes are demonstrated in detail. Also, a reversible intercalation mechanism is confirmed by ex situ X-ray diffraction (XRD), Raman and X-ray photoelectron spectroscopy (XPS) measurements.

The crystal structure of the prepared sample is investigated by XRD and Raman characterizations, as shown in **Figure 1b,c**, respectively. The XRD pattern shows 12 strong characteristic peaks, indicating a high crystallinity of the sample. All peaks are indexed to the orthorhombic crystalline phase of $\text{H}_2\text{V}_3\text{O}_8$ (JCPDS No. 01-085-2401) and no characteristic peaks of impurities are detected. The Raman spectrum of $\text{H}_2\text{V}_3\text{O}_8$ in the range of $100\text{--}1100 \text{ cm}^{-1}$ is shown in **Figure 1c**. Ten peaks, located at $145.8, 179.8, 286.5, 410.5, 505.1, 697.9, 844.4, 881.3, 930.8,$ and 996.5 cm^{-1} , can be assigned to the fundamental modes of $\text{H}_2\text{V}_3\text{O}_8$ orthorhombic crystalline.^[32–34] Two peaks at low-shift of 145.8 and 179.8 cm^{-1} are attributed to the chain translation, which is strongly associated with the layered structure.^[34] The peaks at 286.5 and 410.5 cm^{-1} , $505.1, 697.9, 844.4,$ and 881.3 cm^{-1} are attributed to the bending of $\text{V}2\text{--O}$, the stretching of $\text{V}3\text{--O}$, the stretching of $\text{V}2\text{--O}$, the bending vibration of V--O--V groups, and $\text{V}^{4+}=\text{O}$, respectively.^[32–35] The high-shift peak located at 996.5 cm^{-1} is indexed to the terminal oxygen ($\text{V}=\text{O}$) stretching vibration.^[32] The morphology and microstructure of $\text{H}_2\text{V}_3\text{O}_8$ are investigated by field emission scanning electron microscopy (SEM) and transmission electron

microscopy (TEM). The SEM images (**Figure 1d** and **Figure S2**, Supporting Information) show that the $\text{H}_2\text{V}_3\text{O}_8$ nanowires with a uniform size of $80\text{--}120 \text{ nm}$ in width and several micrometers in length are well dispersed. As is shown in **Figure 1e**, the low-magnification TEM image of $\text{H}_2\text{V}_3\text{O}_8$ shows a highly smooth surface and a similar size to that of SEM images. The high-resolution TEM (HRTEM) image (**Figure 1f**) shows well-resolved lattice fringes, with a regular spacing of 0.341 nm , corresponding to the d_{011} spacing. Besides, the selected area electron diffraction (SAED) pattern, presented in **Figure 1f** (inset), indicates the intrinsic single-crystal structure of $\text{H}_2\text{V}_3\text{O}_8$ which can be well indexed to the orthorhombic structure.

In order to evaluate the electrochemical performances of $\text{H}_2\text{V}_3\text{O}_8$ nanowire electrode, the CR2016 coin-type cells were assembled with metallic zinc as the anode. **Figure 2a** shows the initial three cyclic voltammogram (CV) curves of $\text{Zn}/\text{H}_2\text{V}_3\text{O}_8$ battery at a scan rate of 0.1 mV s^{-1} in the potential range of $0.2\text{--}1.6 \text{ V}$ (vs Zn^{2+}/Zn). There are two pairs of reduction/oxidation peaks at $0.49/0.54$ and $0.73/0.98 \text{ V}$, demonstrating a multi-step reaction mechanism. Meanwhile, the curves of different cycles are mostly overlapped, indicating a reversible process. **Figure 2b** displays the first three charge/discharge profiles at a current density of 0.1 A g^{-1} . The initial three discharge specific capacities are $423.8, 408.4,$ and $402.1 \text{ mA h g}^{-1}$, respectively. The cycling performance of $\text{H}_2\text{V}_3\text{O}_8$ nanowire electrode shows a very high reversible capacity of $\approx 400 \text{ mA h g}^{-1}$ with a retention ratio of 84.5% after 30 cycles and an energy density of $\approx 250 \text{ Wh kg}^{-1}$ at 0.1 A g^{-1} (**Figure S3**, Supporting Information). The cycling behavior of $\text{H}_2\text{V}_3\text{O}_8$ electrode at the current density of 1.0 A g^{-1} is further presented in **Figure 2c,d**. There

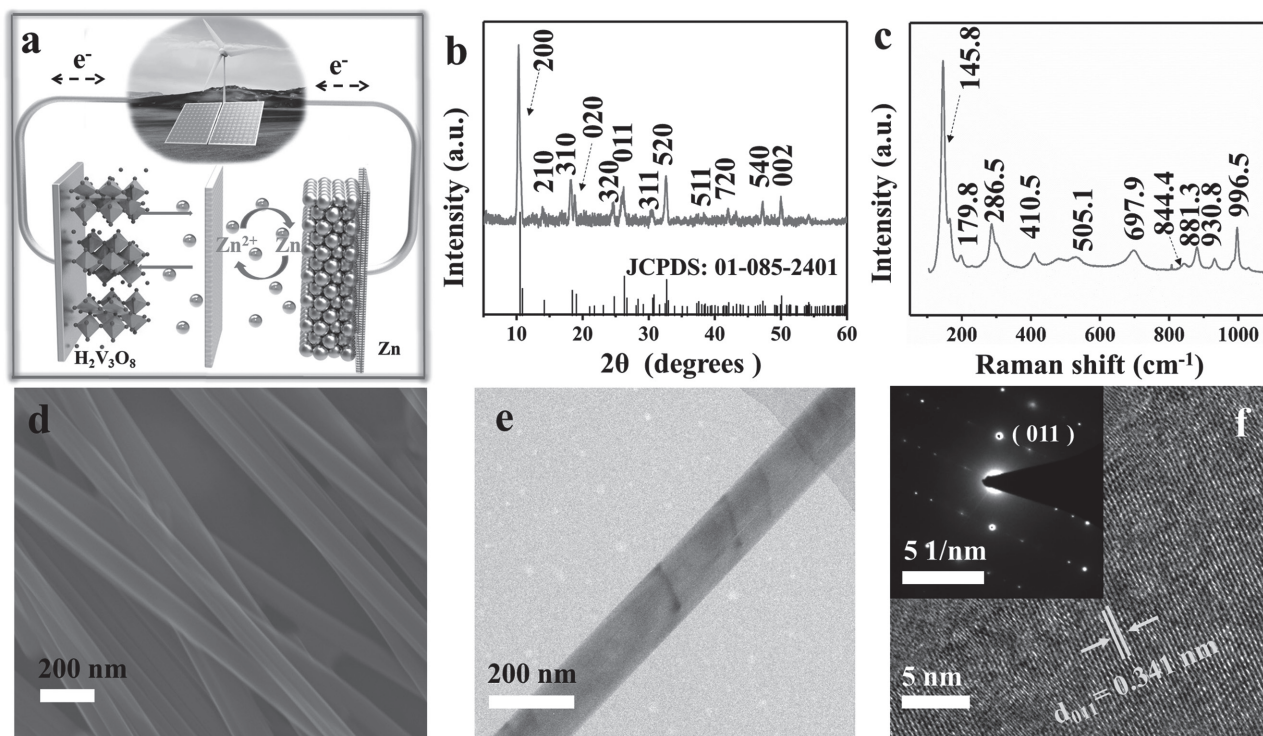


Figure 1. a) Schematic of the rechargeable $\text{Zn}/\text{H}_2\text{V}_3\text{O}_8$ battery, b) XRD pattern, c) Raman spectrum, d) SEM image, e) TEM image, f) HRTEM image (inset: SAED image) of the prepared $\text{H}_2\text{V}_3\text{O}_8$ nanowires.

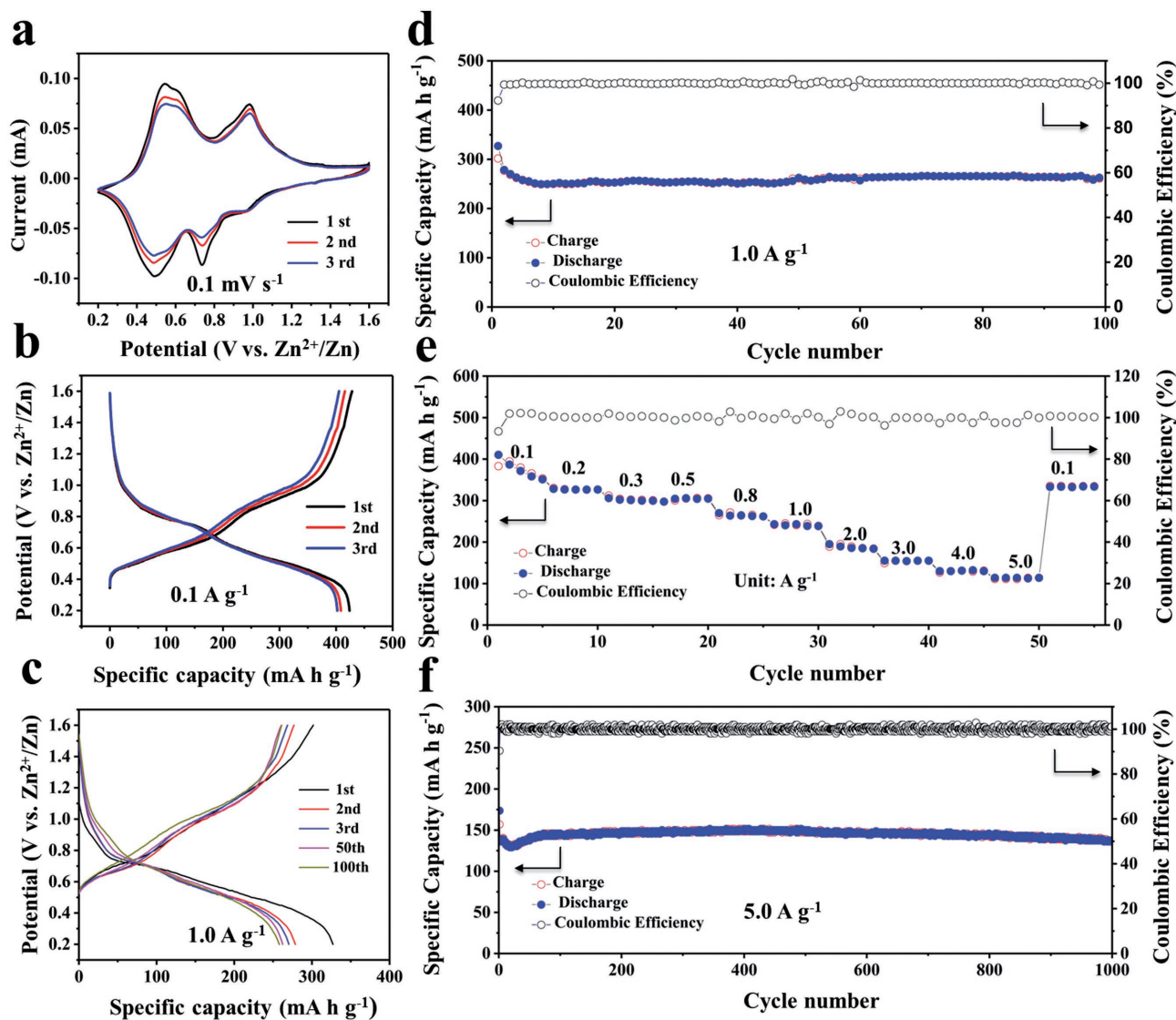


Figure 2. Electrochemical performances of Zn//H₂V₃O₈ battery in the potential range of 0.2–1.6 V. a) CV curves at 0.1 mV s⁻¹ of the initial three cycles. b) Charge/discharge profiles at 0.1 A g⁻¹ of the initial three cycles. c) Charge/discharge curves of different cycles at 1.0 A g⁻¹. d) Cyclic performance at 1.0 A g⁻¹ for 100 cycles. e) Rate performance. f) Prolonged cycle performance at high rate (5.0 A g⁻¹).

are two sloping voltage plateaus in charge/discharge profiles, which are consistent with the two pairs of reduction/oxidation peaks of the CV curves. The discharge capacity (327 mA h g⁻¹) is slightly higher than the charge capacity (301 mA h g⁻¹) of the initial cycle. The reason is that the inserted Zn ions, located at the “dead Zn²⁺ sites”, can’t be extracted from the H₂V₃O₈ lattice during the following charge process.^[35] The similar phenomenon can be found when the other vanadium oxide materials working as cathodes of ZIBs, such as LiV₃O₈ and V₂O₅.^[22,26] The charge/discharge profiles of 2nd, 50th, and 100th cycles maintain a similar shape, and the capacities are 278.6, 262.4, and 258.0 mA h g⁻¹, respectively. The capacity is stabilized at ≈250 mA h g⁻¹ after a slight decrease in the initial eight cycles and the coulombic efficiencies approximate 100% during the first 100 cycles, indicating a high reversibility of the reaction process.

The rate performance of H₂V₃O₈ electrode is investigated at a series of current densities ranging from 0.1 to 5.0 A g⁻¹, as shown in Figure 2e and Figure S4 (Supporting Information). It exhibits discharge capacities of 410.3, 297.4, 240.5, 155.0 mA h g⁻¹ at 0.1, 0.5, 1.0, and 3.0 A g⁻¹, respectively. Even at an extremely high current density of 5.0 A g⁻¹, it also delivers a capacity of 113.9 mA h g⁻¹. When the current density decreases back to 0.1 A g⁻¹, the discharge capacity recovers to 333.7 mA h g⁻¹ with a recovery ratio of 81.3%. All these results show that Zn//H₂V₃O₈ battery has an excellent rate performance, which can meet the requirement of high capacity as well as realize rapid charge/discharge. The prolonged cycling performance of H₂V₃O₈ at high rate (5.0 A g⁻¹) is illustrated in Figure 2f and Figure S5 (Supporting Information). It delivers an initial discharge capacity of 173.6 mA h g⁻¹, and immediately drops to 130.6 mA h g⁻¹ in the following 20 cycles.

Then it begins recovery, and remains steady at approximate 140 mA h g⁻¹, until the 1000th cycle (136.1 mA h g⁻¹) with a capacity retention of 94.3%. The decay of the capacity during the initial 20 cycles is attributed to the fact that the electrolyte gradually penetrated into the interlayer space of V₃O₈ layers at such a high rate. Then, it facilitates the electrochemical reaction, contributing to the increase of capacity in several following cycles. The similar phenomenon is reported in other layered cathode materials for intercalation reaction in alkali ion batteries.^[26,30,35] Moreover, this phenomenon does not appear in the charge/discharge process at the lower current density of 0.1 or 1.0 A g⁻¹, leading to the supposing that the activation of H₂V₃O₈ at 5.0 A g⁻¹ would associate with the kinetics of the electrochemical reaction under high rate solely. The H₂V₃O₈ electrode delivers the highest capacity among the listed systems (Figure S6, Supporting Information) (at the current density of 0.1 A g⁻¹), and the specific capacity does not decrease dramatically when the current density increases from 3.0 to 5.0 A g⁻¹, indicating H₂V₃O₈ is a promising cathode material for ZIBs.

To further investigate the electrochemical kinetics of H₂V₃O₈ electrode, CV measurements at multiple scan rates (from 0.1 to 1.0 mV s⁻¹) were obtained. With the increasing of scan rate, the curves maintain similar shapes and the characteristic peaks become broader (Figure 3a). The reduction and oxidation peaks shift a bit to lower or higher potential, respectively. Generally, the total current (therefore the capacity) is believed to be originated from two independent and distinct parts: surface-induced capacitive process and diffusion-controlled process, as described below:^[31]

$$i = av^b \quad (1)$$

In the above equation, v refers to the scan rate (mV s⁻¹), a and b are adjustable parameters, and b -value ranges from 0.5 to 1.0. When $b = 0.5$, it reveals that the capacity is totally attributed to diffusion controlled process, while $b = 1.0$ indicates a complete capacitive process. Also, b -value can be quantified by the slope of the plot of four redox peaks' log i versus log v (Figure 3b). The fitting results show that the slopes of four redox peaks are 0.73, 0.94, 0.56, and 0.76. The b -value of Peak 2 approximates 1.0, reflecting it is nearly a total capacitive process, and the b -value of Peak 3 is so close to 0.5 that it implies the reaction is almost controlled by diffusion. Furthermore, at a certain scan rate, the capacity can be divided as capacitive (k_1v) and diffusion-controlled ($k_2v^{1/2}$) process at a particular voltage during cycling as described below:^[37]

$$i = k_1v + k_2v^{1/2} \quad (2)$$

$$i/v^{1/2} = k_1v^{1/2} + k_2v^{1/2} \quad (3)$$

For instance, in Figure 3c, at the scan rate of 0.5 mV s⁻¹, the shaded area stands for the surface-induced capacity, accounting for 54.4% of the total capacity. In addition, similar capacity separation curves at other four scan rates are exhibited in Figure S7 (Supporting Information). The contribution ratios of capacitive mechanism at different scan rates are calculated and displayed in Figure 3d. The results show that the capacitive contribution

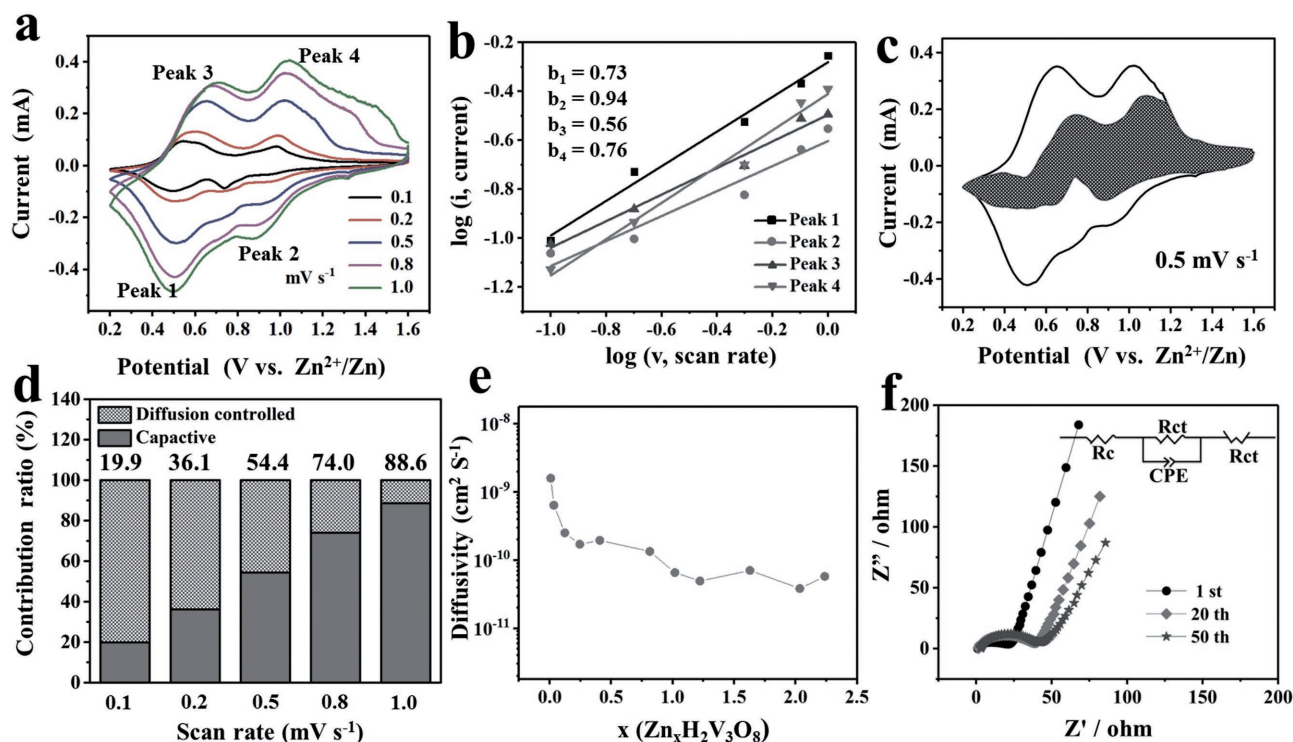


Figure 3. a) CV curves at multiple scan rates. b) Log (i) versus log (v) plots of four redox peaks in CV curves. c) Capacity separation curves at 0.5 mV s⁻¹. d) Capacity contribution ratios at multiple scan rates. e) Diffusivity coefficient at various states of discharge during GITT measurements. f) Nyquist plots of Zn//H₂V₃O₈ battery at different cycles at 1.0 A g⁻¹.

ratio grows from 19.9% to 88.6% with the scan rate rising from 0.1 to 1.0 mV s⁻¹, reflecting that the capacitive controlled process plays the dominant role gradually as the scan rate raise.

Furthermore, the galvanostatic intermittent titration technique (GITT) is used to study the dynamics of Zn²⁺ solid-state diffusion in H₂V₃O₈ lattice. The GITT method is believed to be a standard method for evaluating chemical diffusion coefficients in electrode materials from the potential response to a small constant current pulse. The H₂V₃O₈ electrode exhibits a discharge capacity of 449.0 mA h g⁻¹ in the GITT measurement with the formation of Zn_{2.37}H₂V₃O₈ which possesses maximum zinc ions via a multistep intercalation when discharged to 0.2 V (Figure S8, Supporting Information). Moreover, the Zn²⁺ diffusivity (D^{GITT}) can be calculated by following equation:^[38]

$$D^{\text{GITT}} = \frac{4}{\pi\tau} \left(\frac{m_B V_M}{M_B S} \right)^2 \left(\frac{\Delta E_S}{\Delta E_\tau} \right)^2 \quad (4)$$

where τ represents the constant current pulse time, m_B , V_M , and M_B are the mass loading, the molar volume, and the molar mass of the inserted electrode material, respectively. S is the area of the electrode-electrolyte interface, ΔE_S is the change of steady-state voltage during a single-step GITT experiment, and ΔE_τ stands for the total change of cell voltage during a constant current pulse τ of a single-step GITT experiment regardless of the IR-drop.^[38] As shown in Figure 3e, the diffusion

coefficient of Zn ions in H₂V₃O₈ cathode over the entire intercalation process is in the range of 10⁻¹⁰ to 10⁻⁸. Additionally, there is a tendency that the D^{GITT} becomes smaller gradually, owing to the stronger columbic interaction between each other with the insertion of Zn²⁺ into host material upon discharging. Electrochemical impedance spectroscopy (EIS) is used to gain more insights into the impedance changes of the cycling process at 1.0 A g⁻¹. Figure 3f exhibits the Nyquist plots with a semicircle (at high-frequency) related to charge transfer and a sloped line (Warburg impedance) associated with the transfer of Zn²⁺ (at low-frequency). The intercepts of high-frequency denote innate resistance (R_c). The R_c in the EIS plots of 1st, 20th, and 50th cycle are 0.87, 1.42, and 2.73 Ω , respectively. In case of semicircle radius, it is quantified as R_{ct} to illustrate the charge transfer resistance. It is clear that the R_{ct} of the first cycle (15.97 Ω) is about half of that of the 20th (32.00 Ω), while R_{ct} of the 20th cycle approaches to that of 50th cycle (33.60 Ω). The R_{ct} increase from the 1st to the 20th cycle and is relatively stable from the 20th to the 50th cycle, which may result in the capacity evolution at 1.0 A g⁻¹ that the capacity decreases between the first and the 20th cycle, but the specific capacity difference between the 20th and the 50th cycle is tiny.

The ex situ XRD, TEM, XPS, and Raman tests are applied to explore the reaction mechanism of the Zn//H₂V₃O₈ system upon charge/discharge process. Figure 4a shows the XRD patterns of H₂V₃O₈ electrode at different states, and the

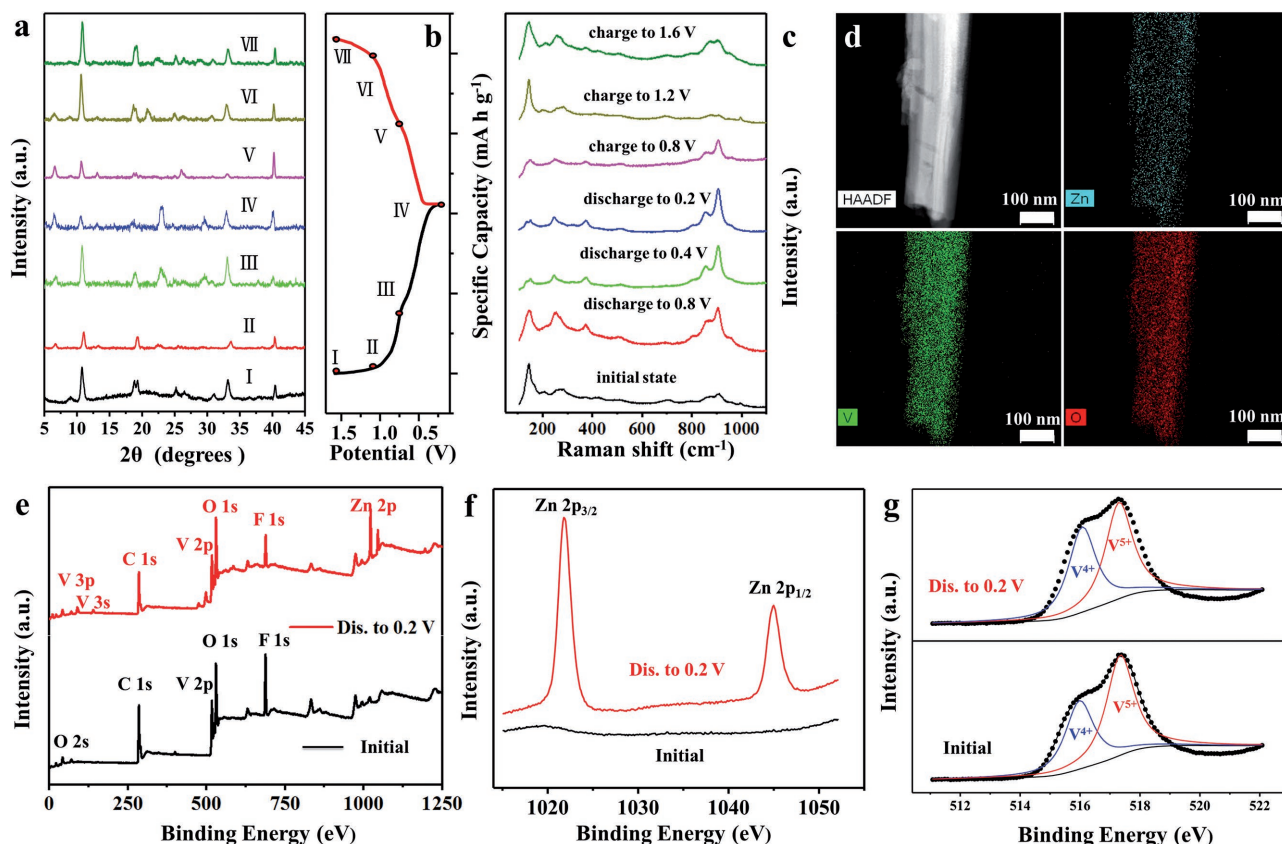


Figure 4. a) Ex situ XRD patterns, and b) corresponding galvanostatic charge and discharge curves at 0.2 A g⁻¹. c) Ex situ Raman spectra of H₂V₃O₈ electrodes at the third cycle. d) TEM-EDX element mapping images at a full discharge state of H₂V₃O₈ electrode after three cycles. e) XPS spectrum of H₂V₃O₈ electrodes, and f) corresponding high resolution XPS spectra of zinc, and g) vanadium at the initial state and the full discharge state.

corresponding galvanostatic charge/discharge curves at 0.2 A g^{-1} of the third cycle is shown in Figure 4b. First, the characteristic diffraction, locates at 10.40° , which corresponds to the crystal face of (200), shifts negatively during the discharge process and then moves positively to the original degree upon charge process. According to Bragg equation, the interlayer spacing of (200) planes (also reflects the lattice constant: a -value) increases during the discharge process and decreases upon charge. Taking the crystal structure of $\text{H}_2\text{V}_3\text{O}_8$ into consideration, the contraction and expansion of a -value should be ascribed to the mobility of Zn^{2+} into the interlayer of V_3O_8 layers. Moreover, a new diffraction emerges when discharged to 0.6 V and disappeared when charged to 1.2 V, which is attributed to the forming/disappearing a new phase of $\text{Zn}_x\text{H}_2\text{V}_3\text{O}_8$ during discharge and charge processes. The diffraction peak at 40.15° belongs to Ti foil which could also be used for calibration. Figure 4c depicts the ex situ Raman spectra of $\text{H}_2\text{V}_3\text{O}_8$ electrode after three cycles at a current density of 0.2 A g^{-1} . The initial stage is roughly the same with that in Figure 1c, indicating negligible structure transform of $\text{H}_2\text{V}_3\text{O}_8$ induced by the insertion and extraction of zinc ions during the first two cycles. The intensity of the peak located at 145.8 cm^{-1} decreases when discharged to 0.2 V and then gradually increases when charged back to 1.6 V, revealing the insertion/extraction of Zn^{2+} in/out of V_3O_8 layers affecting the structure, since this peak is strongly associated with the layered structure. The intensity of the peak at 930.8 cm^{-1} becomes higher during the discharge process, and gets weaker when charged back to 1.6 V. The change of this peak is attributed to the redox of V^{5+} and V^{4+} as the ratio of $\text{V}^{5+}/\text{V}^{4+}$ dropped/increased owing to the redox of V during the insertion/extraction of zinc ions, since this peak is ascribed to $\text{V}^{4+}=\text{O}$.^[34] TEM image, energy dispersive X-ray spectroscopy (EDX) pattern and corresponding elemental mappings of the $\text{H}_2\text{V}_3\text{O}_8$ electrode with Zn intercalation state are shown in Figure 4d and Figure S9 (Supporting Information). The results clearly indicate that elemental Zn is uniformly distributed in the whole nanowire, which confirms the Zn-ion intercalation mechanism. XPS measurements are used to further confirm the de-/insertion mechanism by testing cathode material at initial state and being discharged to 0.2 V later. Figure 4e shows that both cathodes at above two conditions consist of V and O, when discharged to 0.2 V, the peak representing Zn emerges, precisely demonstrating the intercalation of Zn^{2+} into $\text{H}_2\text{V}_3\text{O}_8$. The high-resolution XPS spectrum of Zn element is exhibited in Figure 4f. There is no signal of Zn in the initial state of cathode materials. However, two peaks appear, corresponding to Zn $2p_{3/2}$ and Zn $2p_{1/2}$, when discharged to 0.2 V, accurately declaring the inserting of Zn ions into $\text{H}_2\text{V}_3\text{O}_8$ layered structure. High-resolution XPS spectrum from 1015 to 1055 eV is obtained to analyze the valence state of V (Figure 4g). When discharged to 0.2 V, the intensity of V^{4+} peak strengthened and V^{5+} peak weakened in comparison with the initial state, reflecting the reduction of V^{5+} to V^{4+} along with inserting of zinc ion. In addition, the morphology of $\text{H}_2\text{V}_3\text{O}_8$ nanowire is well preserved even after 100 cycles, indicating a stable layered structure (Figure S10, Supporting Information).

In summary, the $\text{H}_2\text{V}_3\text{O}_8$ nanowires are synthesized through one-step hydrothermal method, and applied to ZIBs as cathode material for the first time. The $\text{Zn}/\text{H}_2\text{V}_3\text{O}_8$ battery delivers a high specific capacity of $423.8 \text{ mA h g}^{-1}$ at the current density

of 0.1 A g^{-1} and a high capacity retention of 94.3% after 1000 cycles at 5.0 A g^{-1} . The electrochemical kinetics of $\text{H}_2\text{V}_3\text{O}_8$ electrodes are demonstrated in detail. Also, a reversible intercalation mechanism is confirmed by ex situ XRD, Raman, TEM, and XPS measurements. Our work demonstrates that $\text{H}_2\text{V}_3\text{O}_8$ is a highly promising cathode material for ZIBs and our investigation on $\text{H}_2\text{V}_3\text{O}_8$ as cathode for ZIBs can be a great motivation for further research on vanadium or other layered structure materials for high-performance ZIBs.

Supporting Information

Supporting Information is available from the Wiley Online Library or from the author.

Acknowledgements

P.H. and Y.L.Q. contributed equally to this work. This work was supported by the National Key Research and Development Program of China (2016YFA0202603, 2016YFA0202604), the Programme of Introducing Talents of Discipline to Universities (B17034), the National Natural Science Foundation of China (51521001, 51602239, 51502227, 51579198), the National Natural Science Fund for Distinguished Young Scholars (51425204), the China Postdoctoral Science Foundation (2015T80845), and the Fundamental Research Funds for the Central Universities (2016111005, 20161VA090, 2017111009, 2017111005, 2017111007, 2017111030), Wuhan Morning Light Plan of Youth Science and Technology (No. 2017050304010316), Prof. Liang He and Prof. Liqiang Mai gratefully acknowledged financial support from China Scholarship Council (Nos. 201606955094, 201606955096).

Conflict of Interest

The authors declare no conflict of interest.

Keywords

$\text{H}_2\text{V}_3\text{O}_8$, intercalation reaction, large-scale energy storage, zinc-ion batteries

Received: July 25, 2017

Revised: August 27, 2017

Published online:

- [1] S. Chu, A. Majumdar, *Nature* **2012**, 488, 294.
- [2] J. B. Goodenough, Y. Kim, *Chem. Mater.* **2010**, 22, 587.
- [3] C. Liu, F. Li, L. P. Ma, H. M. Cheng, *Adv. Mater.* **2010**, 22, 28.
- [4] B. Kang, G. Ceder, *Nature* **2009**, 458, 190.
- [5] W. Tang, Y. Zhu, Y. Hou, L. Liu, Y. Wu, K. P. Loh, H. Zhang, K. Zhu, *Energy Environ. Sci.* **2013**, 6, 2093.
- [6] M. Armand, J. M. Tarascon, *Nature* **2008**, 451, 652.
- [7] C. J. Xu, B. H. Li, H. D. Du, F. Y. Kang, *Angew. Chem., Int. Ed.* **2012**, 51, 933.
- [8] M. C. Lin, M. Gong, B. G. Lu, Y. P. Wu, D. Y. Wan, M. Y. Guan, M. Angell, C. X. Chen, J. Yang, B. J. Hwang, H. J. Dai, *Nature* **2015**, 520, 324.
- [9] Q. An, Y. Li, Y. H. Deog, S. Chen, Q. Ru, L. Mai, Y. Yao, *Nano Energy* **2015**, 18, 265.

- [10] B. F. Ji, F. Zhang, M. H. Sheng, X. F. Tong, Y. B. Tang, *Adv. Mater.* **2016**, *29*, 1604219.
- [11] X. L. Zhang, Y. B. Tang, F. Zhang, C. S. Lee, *Adv. Energy Mater.* **2016**, *6*, 1502588.
- [12] P. P. Qin, M. Wang, N. Li, H. L. Zhu, X. Ding, Y. B. Tang, *Adv. Mater.* **2017**, *29*, 1606805.
- [13] H. Pan, Y. Shao, P. Yan, Y. Cheng, K. S. Han, Z. Nie, C. Wang, J. Yang, X. Li, P. Bhattacharya, K. T. Mueller, J. Liu, *Nat. Energy* **2016**, *1*, 16039.
- [14] B. Li, Z. Nie, M. Vijayakumar, G. Li, J. Liu, V. Sprenkle, W. Wang, *Nat. Commun.* **2015**, *6*, 6303.
- [15] X. Wang, F. Wang, L. Wang, M. Li, Y. Wang, B. Chen, Y. Zhu, L. Fu, L. Zha, L. Zhang, Y. Wu, W. Huang, *Adv. Mater.* **2016**, *28*, 4904.
- [16] D. Kundu, B. D. Adams, V. Duffort, S. H. Vajargah, L. F. Nazar, *Nat. Energy* **2016**, *1*, 16119.
- [17] M. H. Alfaruqi, S. Islam, J. Gim, J. Song, S. Kim, D. T. Pham, J. Jo, Z. Xiu, V. Mathew, J. Kim, *Chem. Phys. Lett.* **2016**, *650*, 64.
- [18] M. H. Alfaruqi, V. Mathew, J. Gim, S. Kim, J. Song, J. P. Baboo, H. C. Sun, J. Kim, *Chem. Mater.* **2015**, *27*, 3609.
- [19] N. Zhang, F. Cheng, Y. Liu, Q. Zhao, K. Lei, C. Chen, X. Liu, J. Chen, *J. Am. Chem. Soc.* **2016**, *138*, 12894.
- [20] L. Zhang, L. Chen, X. Zhou, Z. Liu, *Adv. Energy Mater.* **2015**, *5*, 1400930.
- [21] R. Trócoli, M. F. La, *ChemSusChem* **2014**, *8*, 481.
- [22] P. Senguttuvan, S. D. Han, S. Kim, A. L. Lipson, S. Tepavcevic, T. T. Fister, I. D. Bloom, A. K. Burrell, C. S. Johnson, *Adv. Energy Mater.* **2016**, *6*, 1600826.
- [23] P. He, M. Y. Yan, G. B. Zhang, R. M. Sun, L. N. Chen, Q. Y. An, L. Q. Mai, *Adv. Energy Mater.* **2017**, *7*, 1601920.
- [24] M. H. Alfaruqi, V. Mathew, J. Song, S. Kim, S. Islam, D. T. Pham, J. Jo, S. Kim, J. P. Baboo, Z. Xiu, K. S. Lee, Y. K. Sun, J. Kim, *Chem. Mater.* **2017**, *29*, 1684.
- [25] Y. Oka, T. Yao, N. Yamamoto, *J. Solid State Chem.* **1990**, *89*, 372.
- [26] H. Li, T. Zhai, P. He, Y. Wang, E. Hosono, H. Zhou, *J. Mater. Chem.* **2011**, *21*, 1780.
- [27] Q. An, J. Sheng, X. Xu, Q. Wei, Y. Zhu, C. Han, C. Niu, L. Mai, *New J. Chem.* **2014**, *38*, 2075.
- [28] P. J. Lu, J. Liu, S. Q. Liang, W. J. Wang, M. Leid, S. S. Tang, Q. Yang, *Nano Energy* **2015**, *12*, 709.
- [29] S. Yuan, Y. B. Liu, D. Xu, D. L. Ma, S. Wang, X. H. Yang, Z. Y. Cao, X. B. Zhang, *Adv. Sci.* **2015**, *2*, 1400018.
- [30] S. Sarkar, A. Bhowmik, J. Pan, M. D. Bharadwaj, S. itra, *J. Power Sources* **2016**, *329*, 179.
- [31] D. Wang, Q. Wei, J. Sheng, P. Hu, M. Yan, R. Sun, X. Xu, Q. An, L. Mai, *Phys. Chem. Chem. Phys.* **2016**, *18*, 12074.
- [32] I. Mjejri, N. Ettayeb, F. Sediri, *ChemInform* **2014**, *611*, 372.
- [33] R. Li, Y. C. Liu, *Mater. Res. Bull.* **2010**, *45*, 688.
- [34] X. Zhou, G. Wu, G. Gao, C. Cui, H. Yang, J. Shen, B. Zhou, Z. Zhang, *Electrochim. Acta* **2012**, *74*, 32.
- [35] D. Su, G. Wang, *ACS Nano* **2013**, *7*, 11218.
- [36] G. A. Muller, J. B. Cook, H. S. Kim, S. H. Tolbert, B. Dunn, *Nano Lett.* **2015**, *15*, 1911.
- [37] J. Wang, J. Polleux, A. J. Lim, B. Dunn, *J. Phys. Chem. C* **2007**, *111*, 14925.
- [38] E. Deiss, *Electrochim. Acta* **2005**, *50*, 2927.